

[advances.sciencemag.org/cgi/content/full/6/30/eaba1303/DC1](https://advances.sciencemag.org/cgi/content/full/6/30/eaba1303/DC1)

## Supplementary Materials for

### **Meteorite evidence for partial differentiation and protracted accretion of planetesimals**

Clara Maurel\*, James F. J. Bryson, Richard J. Lyons, Matthew R. Ball, Rajesh V. Chopdekar, Andreas Scholl, Fred J. Ciesla,  
William F. Bottke, Benjamin P. Weiss

\*Corresponding author. Email: [cmaurel@mit.edu](mailto:cmaurel@mit.edu)

Published 24 July 2020, *Sci. Adv.* **6**, eaba1303 (2020)  
DOI: 10.1126/sciadv.aba1303

#### **This PDF file includes:**

Supplementary Text  
Figs. S1 to S8  
Tables S1 to S6  
References

## S1. Silicates in Techado and Colomera

Here we provide a short description of Colomera's and Techado's silicates. The silicates are important to this study for two main reasons. First, the textures of both chondritic and achondritic silicates in the IIEs have been used to infer the thermal evolution of the meteorites. Second, the silicates' compositions establish the identity, and therefore closure temperature, of the dominant Ar-bearing phase that has been dated using  $^{40}\text{Ar}/^{39}\text{Ar}$  chronology of bulk samples. Because the closure temperatures for Colomera and Techado are similar to the temperature at which tetraenaite forms, the  $^{40}\text{Ar}/^{39}\text{Ar}$  ages correspond to the time of acquisition of their NRM (see main text).

Colomera's achondritic silicates are multiphase assemblages ranging in diameter up to ~5 mm and composed mainly of 70 vol. % plagioclase and ~30 vol. % clinopyroxene and orthopyroxene (31). The additional presence of feldspathic glasses in Colomera indicates quenching (cooling at  $> 10^{10} \text{ }^\circ\text{C My}^{-1}$ ) to near or below their solidus at 850–1000°C. The presence of glasses of similar composition in several IIEs argues in favor of a large early impact exposing melted silicates to near-surface temperatures (of the order of ~100°C) (18).

To explain the presence of cloudy zones (CZs) in the matrix metal of Colomera (and Techado), this period of fast cooling must have been limited and followed by slow cooling ( $< 10,000^\circ\text{C My}^{-1}$ ). Time-temperature-transformation diagrams obtained from devitrification experiments on tektites (with a similar composition as Colomera's glasses) demonstrate that if Colomera's glasses were quenched below 850°C, they would not have devitrified during the subsequent slow-cooling episode ( $\sim 2.5^\circ\text{C My}^{-1}$  at  $\sim 350^\circ\text{C}$ ; Section S10) (5:).

Techado contains one cm-sized, near-chondritic silicate inclusion with a dominant mixture of olivine and pyroxene (~80 vol.%) along with plagioclase (~20 vol.%) (31). The shape of the silicate and coarseness of its constituent grains suggest that Techado experienced heating, but did not reach the solidus temperature of its silicates (18).

## S2. Siderophile element pattern of the IIE meteorites

Iron-meteorite groups that formed by fractional crystallization of a metallic core exhibit a strong negative trend in highly refractory siderophile element concentrations (e.g., Ir) versus volatile siderophile element concentrations (e.g., Au) that spans several orders of magnitude (5:). This trend reflects increasing degrees of closed system fractional crystallization of a core. For example, IIAB meteorites, thought to have formed in a fractionally crystallizing metallic core, have Ir concentrations ranging from 0.01 to 60  $\mu\text{g/g}$  for Au ranging from 0.5 to 2  $\mu\text{g/g}$  (5:). This is not the case for the IIEs, whose Ir composition extends from just 1 to 8  $\mu\text{g/g}$  over approximately the same range of Au concentrations.

This absence of correlation between Au and Ir has been interpreted as evidence that the IIEs did not crystallize within the core of their parent body (20). Instead, ref. (20) proposed that the mixing occurred at the bottom of impact craters on a metal-rich, undifferentiated body. In that case, the degree of metamorphism of the IIE chondritic silicate as well as the melting of their achondritic silicates could either be a consequence of the strong temperature gradient in the metal pools or be the result of multiple impacts producing different level of heating. Petrological evidence, in particular the fact that achondritic silicates are close to equilibrium melts, appear to be incompatible with this scenario (18). Additionally, our newly measured cooling rates at  $\sim 350^\circ\text{C}$  of the IIEs are only a few degrees per million years (section S10), which requires that the meteorites were buried under a significant layer of isolating material and is incompatible with the fast cooling expected at the bottom of impact craters.

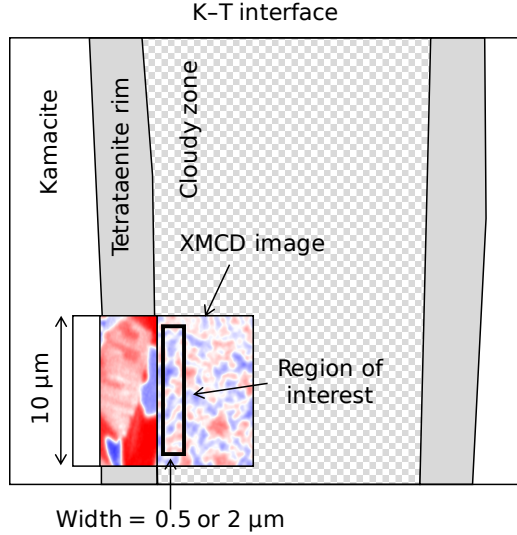


**Fig. S1. Diagram showing various quantities associated with XPEEM measurements.** A K–T interface refers to the combination of tetraetaenite rims and CZs (entire box). The region of interest has a width of ~500 nm and is located next to the tetraetaenite rim for Techado. It has a width of ~2 μm and is located next to the rim for Colomera (see sections S3 and S8 for details). Multiple XMCD images are acquired along one side of the K–T interface.

### S3. X-ray photoemission electron microscopy (XPEEM) measurements

#### a) Correction of the raw XPEEM images for Colomera

The XPEEM protocol including the acquisition of off-edge images described in the main text Materials and Methods was strictly applied for our last measurement campaign conducted for Techado. For our earlier measurements of Colomera, off-edge images were recorded only during our second series of measurements (i.e., K–T interfaces A, B and C) but not the first (i.e., K–T interface D). We also monitored the incoming X-ray intensity,  $I_0$ , for these two series of measurements. When off-edge images were available, we did subtract them from the corresponding on-edge images. For consistency across all K–T interfaces of Colomera, we chose to only divide each subtracted XPEEM image by this value:

$$I_{\text{corr}_i0}^{\pm} = \frac{I_{\text{on-edge}}^{\pm} - I_{\text{off-edge}}^{\pm}}{I_0} \quad (\text{S1})$$

where  $I_{\text{on-edge}}^{\pm}$  and  $I_{\text{off-edge}}^{\pm}$  are the pixel intensities obtained with a left- and right-circularly polarized beam tuned to on-edge and off-edge energies, respectively.

#### b) Selection of the region of interest

To include in our datasets only the coarsest islands, which are located close to the rim, we calculated the average XMCD intensities in a 0.5-μm large region of the CZ next to the tetraetaenite rim for Techado while for Colomera, we used a 2-μm large region next to the rim. The motivation for these sizes is that we seek to minimize the island size variation across one region (since our paleointensity calculations assume this is constant; see equation S2) while maximizing the number

of islands to minimize the statistical uncertainties associated with finite numbers of islands (section S6b). Our SEM measurements of both meteorites confirm that island sizes are essentially constant across both selected regions (section S8). By choosing regions next to the rim, we also avoided working with the smallest CZ islands formed below  $\sim 34$  wt.% Ni, whose magnetization acquisition process remains poorly understood. In all the region of interest analyzed in both meteorites, the Ni local concentration was higher than 34 wt.%, so that the islands formed above the tetraenaite ordering temperature.

### c) Theoretical Maxwell-Boltzmann approach

Because the XMCD contrast of individual CZ islands is not spatially resolved, we compare the XMCD data to that expected for a Maxwell-Boltzmann distribution of the average magnetization directions (14). In particular, we account for the fact that each island's magnetization can adopt one of the six preferred directions of tetraenaite (see main text Materials and Methods) whose probability depends on the direction of the field experienced as tetraenaite formed. Each CZ island has a magnetization  $M_s V$ , where  $M_s$  is the tetraenaite saturation magnetization ( $1300 \text{ kA m}^{-1}$ ) and  $V$  is the volume of the island at the time the field is recorded, oriented along one of the six preferred directions, denoted  $\pm x$ ,  $\pm y$  and  $\pm z$ . The associated magnetostatic energies in the presence of an external ancient magnetic field  $B = (B_x, B_y, B_z)$  are given by:

$$\begin{aligned} E_{\pm x} &= \pm M_s V B_x \\ E_{\pm y} &= \pm M_s V B_y \\ E_{\pm z} &= \pm M_s V B_z \end{aligned} \quad (\text{S2})$$

The Ni-poor matrix that surrounds the islands is paramagnetic (22). As a consequence, it may contribute to the magnetic energy budget with a component induced by the field generated by the islands. However, this induced field would be proportional to the paramagnetic susceptibility, meaning it would be  $\sim 10^{-3}$  times less intense than the islands' field (82). It is therefore not accounted for in our calculations.

In the Maxwell-Boltzmann framework, the probability  $p_i$  that the magnetization of an island adopts direction  $i$  equals the ratio of the number of islands adopting this direction ( $n_i$ ) to the total number of islands ( $n$ ):

$$p_i = \frac{n_i}{n} = \frac{\exp\left(-\frac{E_i}{k_B T}\right)}{\sum_{j=1}^{j=6} \exp\left(-\frac{E_j}{k_B T}\right)} \quad (\text{S3})$$

where  $T$  is the ordering temperature of tetraenaite [ $320^\circ\text{C}$  (24)]  $k_B$  is Boltzmann's constant and  $j = \pm x, \pm y$  or  $\pm z$ . Moreover, the average XMCD intensity measured across a region of the CZ ( $I_{\text{XMCD,CZ}}$ ) can be written as the sum of the six possible XMCD intensities,  $I_{\text{XMCD},i}$ , corresponding to the six magnetic easy axes of tetraenaite weighted by the probability  $p_i$  that an island adopts this specific orientation:

$$I_{\text{XMCD,CZ}} = \sum_{i=1}^{i=6} p_i I_{\text{XMCD},i} \quad (\text{S4})$$

Substituting eq. (S3) into eq. (S4), we obtain an equation relating the XMCD intensities experimentally measured with XPEEM and the three components of the putative ancient field that magnetized the meteorite:

$$I_{\text{XMCD,CZ}} = \frac{\sum_{i=1}^{i=6} I_{\text{XMCD},i} \exp\left(-\frac{E_i}{k_B T}\right)}{\sum_{i=1}^{i=6} \exp\left(-\frac{E_i}{k_B T}\right)} \quad (\text{S5a})$$

With the XMCD intensities measured for three different orientations of the sample with respect to the X-ray beam direction (namely  $I_{\text{XMCD},i}$ ,  $I'_{\text{XMCD},i}$ ,  $I''_{\text{XMCD},i}$ , and  $I_{\text{XMCD,CZ}}$ ,  $I'_{\text{XMCD,CZ}}$ ,  $I''_{\text{XMCD,CZ}}$ ) we obtain a system of three equations [see equations (4-6) of ref. (14)].

$$I'_{\text{XMCD,CZ}} = \frac{\sum_{i=1}^{i=6} I'_{\text{XMCD},i} \exp\left(-\frac{E_i}{k_B T}\right)}{\sum_{i=1}^{i=6} \exp\left(-\frac{E_i}{k_B T}\right)} \quad (\text{S5b})$$

$$I''_{\text{XMCD,CZ}} = \frac{\sum_{i=1}^{i=6} I''_{\text{XMCD},i} \exp\left(-\frac{E_i}{k_B T}\right)}{\sum_{i=1}^{i=6} \exp\left(-\frac{E_i}{k_B T}\right)} \quad (\text{S5c})$$

All parameters in eq. (S5a–c) are known: the ordering temperature, saturation magnetization, and island size at blocking temperature (with the latter obtained using the cloudy zone formation model described in Section S9). We can therefore solve the system to obtain the three components  $B_x$ ,  $B_y$  and  $B_z$  of the ancient field relative to the three preferred directions of tetrataenite.

#### S4. Electron backscatter diffraction (EBSD) measurements

Because dynamo fields are homogenous on spatial scales far exceeding that of meteorite hand samples, a key quality of NRM acquired in an ancient field at a single time is that it should be unidirectional across all K-T interfaces of a given sample. Therefore, it is important to obtain the absolute orientations of the NRM in the interfaces in each meteorite. However, our XPEEM analysis recovers the projection of the ancient field direction onto the three possible easy axis orientations of the local tetrataenite grains. Given that we analyzed K–T interfaces that formed up to ~5 mm apart, these tetrataenite phases might have been derived from different parent taenite grains with differing crystallographic orientations. Hence, determination of the absolute

orientation of the crystal lattices of the analyzed K–T interfaces is required to test for unidirectionality of the NRM.

To obtain the crystallographic orientations of the K–T interfaces studied with XPEEM, we used EBSD with a tilt angle of 70°, an acceleration voltage of 20 kV and incident beam currents of 5 nA. The measured diffraction patterns were compared to the  $\alpha$ -bcc iron reference for kamacite and  $\gamma$ -fcc iron reference for taenite/tetrataenite. For Colomera, the measurements were conducted using the Zeiss Merlin Scanning Electron Microscope at the MIT Material Science Department and the data analysis used the Orientation Imaging Microscopy (OIM) Analysis software. For Techado, we used the FEI Quanta 650F SEM at the Department of Materials Science and Metallurgy, University of Cambridge combined with the Brukers ESPRIT software for data analysis.

For Colomera, we measured the orientation of the  $\langle 100 \rangle$  directions for all K–T interfaces, interface D being located on the opposite face of the sample with respect to the others (main Fig. 2). We found that the  $\langle 100 \rangle$  directions of each CZ, once rotated into a common reference frame, are essentially unidirectional (Fig. S2A–B), implying that the directional data obtained from XPEEM do not need to be rotated to mutually orient the crystallographic axes of tetrataenite. We drew the same conclusion for the two CZs measured in Techado (Fig. S2C). Therefore, the CZs formed from a single parent taenite crystal within each meteorite.

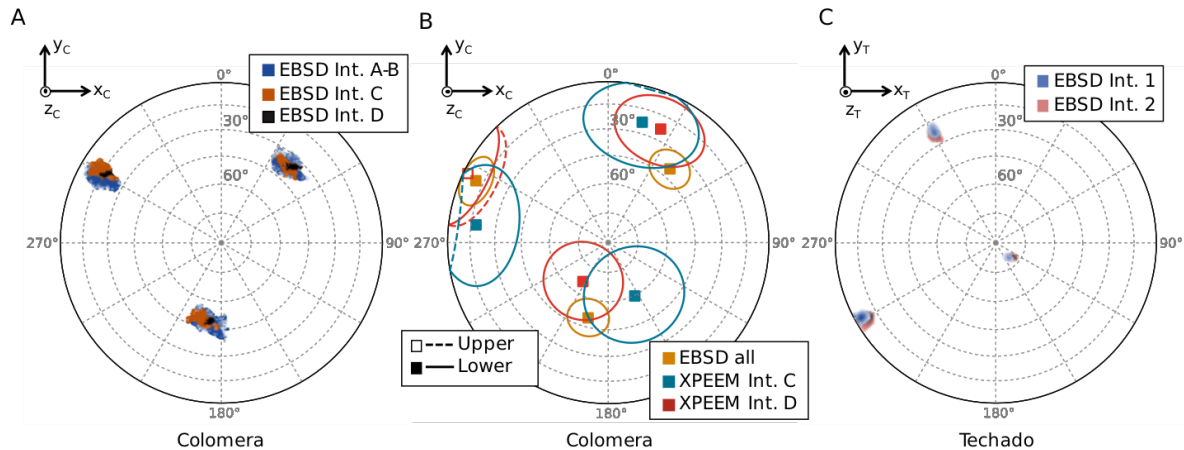


**Fig. S2. Mutually orienting the K-T interfaces within Colomera and Techado.** (A) Equal area projection of the  $\langle 100 \rangle$  directions in the K–T interfaces (i.e., tetrataenite rim and CZ) measured with EBSD for all four interfaces in Colomera. The easy axes of interface D were measured in a different sample orientation and are rotated into the same reference frame as the other interfaces on this figure. Only three of the six directions are shown (the other three being opposite to those shown here) (B) Equal area projection of the easy axis directions estimated from XMCD intensities for interfaces C and D in Colomera. For clarity, we did not include interfaces A and B, and show only three directions. The easy axis directions (same for all interfaces) measured with EBSD are shown for comparison, with a confidence ellipse representing the spread estimated from (A). Ellipses represent the 95% confidence intervals, calculated by bootstrapping for the XMCD-derived directions or estimated from EBSD measurements. (C) Equal area projection of the  $\langle 100 \rangle$  directions in the tetrataenite rim and CZ measured with EBSD for the two interfaces in Techado. Only three directions are shown. In (A–C), open (closed) symbols and dashed (solid) lines denote upper (lower) hemisphere. The reference frames refer to main Fig. 2.

## S5. Statistical tests for unidirectionality

In this section, we consider whether the measured XMCD intensities exclude the possibility that tetraenaite in CZ islands formed in the absence of a field (section S5a). We then explain the statistical tests that allow us to conclude that all CZs in one meteorite were likely magnetized by the same field (section S5b).

### a) Directional bias in the cloudy zones

If a CZ grew in the presence of a magnetic field, we expect a bias in the distribution of CZ island magnetizations towards the easy axis closest to the external field direction (63) [see equation (S3)]. Conversely, if the CZ cooled in the absence of a field or experienced a very weak field, equal distributions along each of the possible easy axes are expected. To assess whether the CZs in our samples experienced an ancient field, we first compared the net magnetization measured for a region of interest to the net magnetization expected if the individual island magnetizations were evenly distributed along the three preferred magnetization directions. We used a bootstrapping method in three steps:

- 1) We choose (with replacement) among the average XMCD intensities measured in the region of interest in a given CZ and a given orientation of the sample. We repeat as many times as there are XMCD images for the given CZ in our dataset. We calculate the mean of these values. We repeat 1,000 times.
- 2) Using the characteristic XMCD intensities measured in the tetraenaite rim, calculate what would be the average XMCD value of this region of the CZ assuming equal partition of the magnetization directions along the three easy axes. To do this, we estimate first the number of islands in the region of interest. We do so by using the island size measured from SEM images and the fact that islands occupy ~90% of the given region of the CZ (Section S9; Fig. S7). We then assign randomly one of the six XMCD intensities measured in the rim. We repeat as many times as there are XMCD images for the given CZ in our dataset. We then calculate the mean of these values. We repeat this 1,000 times.
- 3) Finally, we compare the 95% confidence intervals (i.e., the range of values that contain 95% of the mean XMCD values calculated above) of the measured data (from step 1) with that of the simulated random distribution (from step 2).

We found that all CZs studied have, for at least one orientation of the sample, a measured distribution that does not overlap with the simulated random distribution interval to 95% confidence (Fig. S3), implying that each CZ exhibits a significant bias in the distribution of island magnetization directions. This in turn implies that the CZ islands included in our datasets acquired their magnetization in the presence of a non-zero magnetic field.

In our Maxwell-Boltzmann framework, the paleointensity derived from an XPEEM dataset is obtained by combining the XMCD intensities of the rim and of the region of interest in the CZ. Non-overlapping confidence intervals in the XMCD intensity space between our data and simulated zero-field data (Fig. S3) will therefore automatically yield non-overlapping confidence intervals in the paleointensity space.

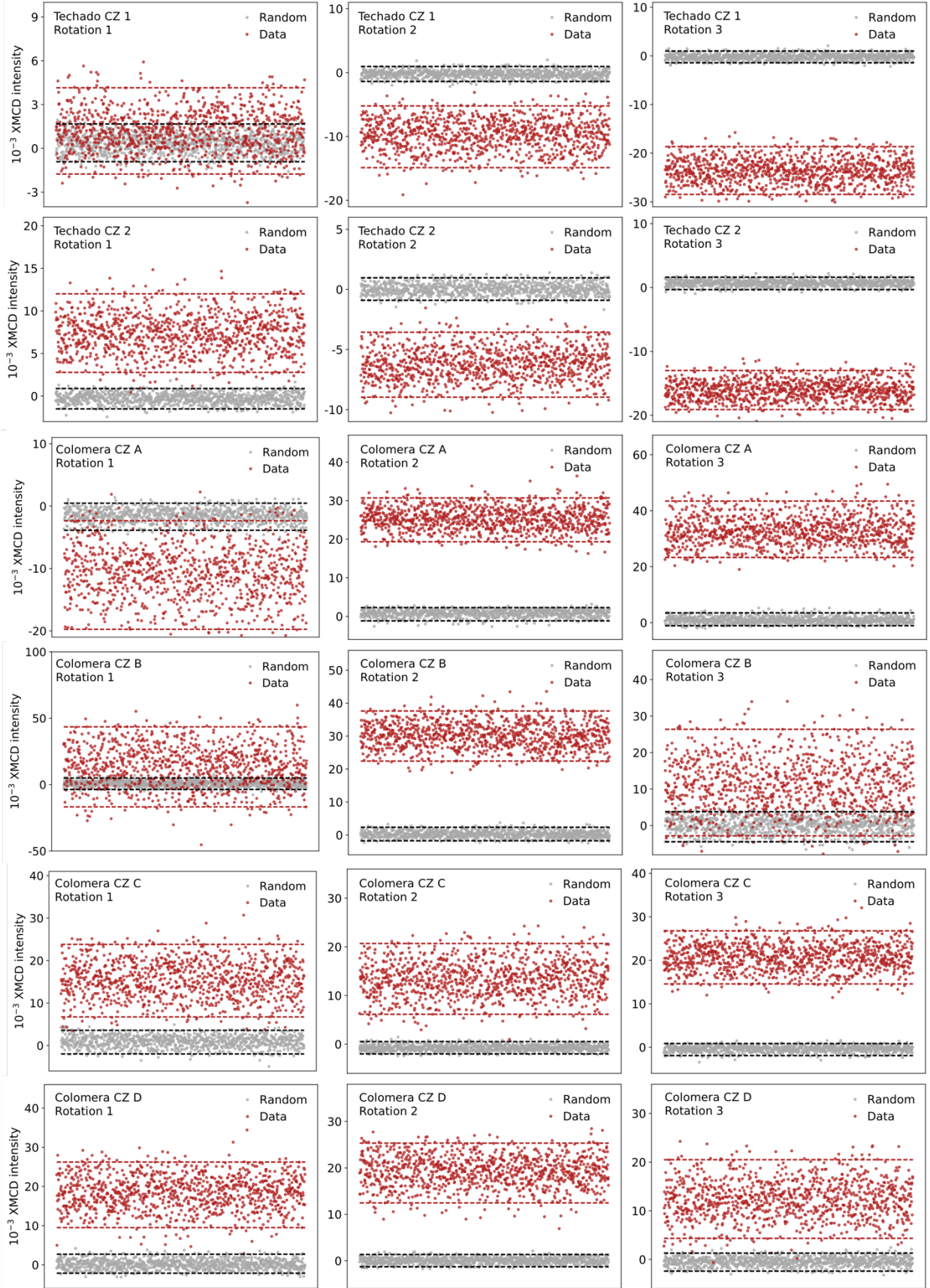


**Fig. S3. Demonstration that NRM in Techado and Colomera was acquired in a non-zero field.** Distribution of the average XMCD intensity of each CZ analyzed in Techado and Colomera obtained by bootstrapping for the three different sample orientations (red dots), compared to the distribution obtained with a random distribution of the magnetization directions along one of the six easy axis directions (grey dots). Dashed lines show the 95% confidence interval of each distribution. The means obtained after each of the thousand trials are distributed along the abscissas of the figures.

b) Watson’s test and  $V_w$  statistical test

Here we describe two statistical tests conducted on each XPEEM dataset. The first is Watson’s test for randomness (64), which establishes whether a distribution of directions (i.e., the field orientations estimated from each XMCD image of one K–T interface) are drawn from a uniform distribution. The second is the  $V_w$  test, which assesses whether two Fisher-distributed three-dimensional distributions of unit vectors (i.e., mean directions of two K–T interfaces from a given meteorite) share a common mean direction. It allows us to determine whether, within a given confidence interval, all CZs studied in one meteorite exhibit a common paleodirection.

For Watson’s test, we compared the set of directions calculated from each set of XMCD images of a given K–T interface to a uniform distribution on a sphere. We found that each dataset for each K–T interface studied was not drawn from a random distribution at 99% confidence (Table S1). The second test consisted of calculating the  $V_w$  statistic (65) for each pair of K–T interfaces within a given meteorite and comparing them to a critical value. The critical value of the  $V_w$  statistic is obtained in three steps: 1) simulate two Fisher distributions with the same number of points and same dispersion as the two experimental datasets, but with a common true mean direction; 2) calculate their  $V_w$  statistic; 3) repeat this operation a thousand times and take the 950<sup>th</sup> greatest value of  $V_w$ . If this critical value is larger than the  $V_w$  statistic for the pair, the hypothesis that the two experimental distributions have the same mean direction cannot be rejected at 95% confidence. We found that the differences in the mean paleodirections estimated from K–T interface A, B, C and D in Colomera, as well as CZ 1 and 2 in Techado, are not significant to 95% confidence (Table S2).

Meteorite	K–T interface	$N$	$R$ or $\sqrt{3R^2/N}$	$R_0$ or $\chi_3^2$ (99% confidence)
Techado	1	25	29.2	11.34
	2	33	102.3	7.81
Colomera	A	7	7.6	5.26
	B	8	6.7	4.89
	C	10	17.2	11.34
	D	13	22.4	11.34

**Table S1. Calculated statistics and critical values for Watson’s test.** Parameters for a test of uniformity against a unimodal alternative (64, 66). The first two columns indicate the meteorite and the K–T interface considered. The third column gives the number of locations analyzed (i.e.,

data points obtained) on each interface. The fourth column shows the resultant length of the data  $R$ , if  $N < 10$  or the value  $\sqrt{3R^2/N}$  if  $N \geq 10$ . This value is compared to the critical value in the fifth column, namely  $R_0$  if  $N < 10$  and  $\chi_3^2$  if  $N \geq 10$ . If  $R > R_0$  or  $\sqrt{3R^2/N} > \chi_3^2$ , the uniformity hypothesis can be rejected at 99% confidence.

Pair of K–T interfaces	$V_w$	Critical $V_w$ 95% confidence	Pair of CZs	$V_w$	Critical $V_w$ 95% confidence
B – C	1.61	6.51	A – B	5.08	7.61
B – D	0.40	8.80	A – C	0.68	9.28
C – D	5.07	10.92	A – D	5.77	6.99
1 – 2	2.3	37.0			

**Table S2. Calculated statistics and critical values for the  $V_w$  statistical test.** The first and fourth columns indicate the pair of K–T interfaces compared (A, B, C and D for Colomera, 1 and 2 for Techado). The second and fifth columns give the  $V_w$  statistics calculated for each pair. If the  $V_w$  value is smaller than its critical value given by the third and sixth columns, we cannot reject at 95% confidence the hypothesis that the field directions recovered from the two CZs are equivalent. It is the case for all pairs in both meteorites.

### S6. Uncertainties in paleodirection and paleointensity

Here, we estimate the uncertainties on the paleodirection and paleointensity inherent to our measurements. These are due to experimental measurement noise such as time-dependent drifts of the incoming X-ray beam or varying resolution of the instrument’s electron optics (section S6a), counting statistics associated with the limited number of islands included in a given XPEEM dataset (section S6b), and rotation of Colomera’s data into a common reference frame (section S6c). Tables S4 and S5 summarize the results.

#### a) Measurement noise

To quantify the measurement uncertainty, we proceeded by bootstrapping in a similar fashion as step 1) of section S5a. Among the measured XMCD quantities, we picked with replacement as many values as the number of locations we analyzed along a given K–T interface. This was done for each rim XMCD intensity and each average CZ XMCD intensity, for a total of seven values. We then calculated the average paleodirection and paleointensity for this dataset using Eq. (S5). This was repeated a thousand times. The 95% confidence interval in paleodirection is quantified by the cone that contains 95% of the mean directions calculated. The 95% confidence interval in paleointensity contains 95% of the paleointensity values calculated.

#### b) Small-number statistical uncertainty

The small-number statistical uncertainty results from counting statistics associated with the finite number of islands included in each XPEEM dataset. It quantifies how well the paleodirection estimated from a CZ reflects the relative orientation of the ancient field. An analytical formula for

this uncertainty has been calculated in the Maxwell-Boltzmann framework by ref. (67) for the field direction (eq. S6a) and intensity (eq. S6b):

$$\alpha_{95} = \tan^{-1} \left( \sqrt{\frac{8\pi}{3N} \frac{k_B T_B}{\mu_0 H_0 V_B M_{S,B}}} \right) \quad (\text{S6a})$$

$$\delta m = \sqrt{\frac{3}{N} \frac{k_B T_B}{\mu_0 H_0 V_B M_{S,B}}} \quad (\text{S6b})$$

where  $\alpha_{95}$  is the half cone 95% confidence directional uncertainty,  $\delta m$  is the 95% confidence uncertainty in paleointensity,  $N$  is the number of CZ islands included in the dataset,  $T_B$  is the blocking temperature (320°C),  $\mu_0 H_0$  is the intensity estimate for the ancient magnetic field,  $V_B$  is the volume of the CZ islands at tetraenaite ordering temperature,  $M_{S,B}$  is the saturation magnetization at blocking temperature and  $k_B$  is Boltzmann's constant.

Equations (S6a-b) show that the small-number statistical uncertainty inversely depends on the size of CZ islands at their blocking temperature for small values of  $\alpha_{95}$ . Larger islands have larger magnetic moments and couple more strongly to an external field; in this case a smaller number of islands is necessary to obtain the same net magnetization. We estimated this size using the model described in Section S9. The equations also show that the small-number statistical uncertainty inversely depends on the intensity of the ancient field. If the ambient field is weak, more islands are needed in the dataset for their net moment to reliably match the field orientation. We used the average field intensities estimated from XPEEM measurements for each CZ and the approximate number of CZ islands included in each XPEEM dataset in eq. (S6a) and (S6b). The small-number statistical uncertainties in direction (resp. intensity) for all CZ studied in both meteorites range between 6° and 10° (resp. 7% and 10%) for Colomera and are within 4° and 5° (resp. 5%) for Techado (Table S3). This small-number statistical uncertainty was added to the total uncertainty estimated for each XPEEM dataset.

<b>Meteorite</b>	<b>Interface</b>	<b>Approximate number of islands in XPEEM dataset</b>	<b>Average field intensity estimate (<math>\mu\text{T}</math>)</b>	<b>Statistical uncertainty in direction (<math>^\circ</math>)</b>	<b>Statistical uncertainty in intensity (%)</b>
Colomera	A	1090	13	9	10
	B	954	20	6	7
	C	1363	14	8	9
	D	1772	10	10	10
Techado	1	1200	35	5	5
	2	1600	36	4	5

**Table S3. Small-number statistical uncertainty for each CZ analyzed.** The first and second columns give the name of the meteorite and which K–T interface is considered. For each CZ found in the given interface, the third column shows the approximate number of islands in the XPEEM dataset calculated using the measured average island size, the width of the CZ region of interest (0.5- $\mu\text{m}$  for Techado, 2- $\mu\text{m}$  for Colomera) and assuming the islands occupy 90% of the region. The fourth column shows the average field intensity estimated assuming an underlying Maxwell-Boltzmann distribution for individual islands' magnetizations. The fifth and sixth columns provide the statistical uncertainty in direction and intensity calculated with Eq. (S6a) and (S6b), respectively.

c) Island size at tetrataenite formation temperature

Given our uncertainty on the local Ni content in the regions of the CZ included in our datasets, our knowledge of the size of the islands at 320°C also has an uncertainty. A  $\pm 1$  wt.% uncertainty in Ni content, which is a relatively large estimate given the Ni profiles measured (Fig. S5), propagates into a 5% uncertainty on the size of the islands at 320°C (28). Because the paleointensity estimate depends on the volume of the islands, this results in an additional 15% uncertainty on the paleointensity. To be conservative, we included this uncertainty in our final estimates.

d) Additional directional uncertainty for Colomera

The measurements of K–T interface D in Colomera were acquired with a different sample orientation than those of interfaces A, B and C. To measure interface D with XPEEM, the rectangular sample was flipped about its small axis and rotated by  $\sim 15^\circ$  clockwise (main Fig. 2). The rotation of the inferred NRM directions, initially estimated in the reference frame of the tetrataenite easy axes, introduces a directional uncertainty that needs to be quantified. The coordinates of each easy axes in a chosen reference frame can be determined using the XMCD intensities collected in the tetrataenite rim:

$$\begin{aligned} \mathbf{e}^i \cdot \mathbf{k} &\sim a I_{\text{XMCD},i} \\ \mathbf{e}^i \cdot \mathbf{k}' &\sim a' I'_{\text{XMCD},i} \\ \mathbf{e}^i \cdot \mathbf{k}'' &\sim a'' I''_{\text{XMCD},i} \end{aligned} \quad (\text{S7})$$

where  $\mathbf{e}^i$  is the unit vector for the easy axis  $i$ ;  $\mathbf{k}$ ,  $\mathbf{k}'$  and  $\mathbf{k}''$  are the unit vectors aligned with the beam directions for each of the three orientations of the beam with respect to the sample; and  $I_{\text{XMCD},i}$ ,  $I'_{\text{XMCD},i}$  and  $I''_{\text{XMCD},i}$  are the tetrataenite rim XMCD intensities corresponding to easy axis  $i$  for each of the three orientations of the beam with respect to the sample. The proportionality factors  $a$ ,  $a'$  and  $a''$  are unknown. To evaluate the error induced by this factor on the easy axis directions, we proceeded by bootstrapping as follows:

- 1) We assign a value to the unknown factor picked randomly between 0.01 and 5 and divide the measured XMCD intensity. The upper value is chosen because maximum XMCD values are  $\sim 0.2$  and the dot product between two unit vectors has to remain smaller than 1. The lower bound is arbitrary; picking smaller values does not affect the final confidence interval.
- 2) We calculate the easy axis directions using eq. (S7) and find the closest set of three orthogonal vectors;
- 3) We repeat this sequence 1,000 times.

The easy axes directions found with this method, once rotated in a common reference frame, are close to the directions measured with EBSD (Fig. S2B). For each K–T interface, 95% of the axes obtained by bootstrapping were within a 20° to 25° cone. This uncertainty was added to the total uncertainty of the paleodirection estimated from the interfaces in Colomera.

Meteorite	K–T Int.	Paleodirection (°)				
		Declination Inclination	Measurement uncertainty	Small-number statistical uncertainty	Orientation uncertainty	Total uncertainty
Colomera	A	168.3 41.1	27	9	23	37
	B	242.5 47.9	34	6	23	42
	C	199.7 58.8	28	8	25	38
	D	22.3 85.1	29	10	20	37
Techado	1	6.05 -75.4	12	5	0	13
	2	338.2 -70.6	14	4	0	14.5

**Table S4. Average estimated paleodirections and associated uncertainties.** The first and second columns give the name of the meteorite and which K–T interface is considered. The third column shows the average declination and inclination obtained from bootstrapping, in the reference frames of main Fig. 2. The fourth, fifth and sixth columns give the measurement uncertainty, small-number statistical uncertainty and orientation uncertainty, respectively (section S6). The total uncertainty in paleodirection is given in the seventh column. All uncertainties refer to the angle of the 95% confidence cones.

Meteorite	K–T Int.	Paleointensity ( $\mu\text{T}$ )				
		Average intensity	Measurement uncertainty	Small-number statistical uncertainty	Island size estimate uncertainty	Total uncertainty
Colomera	A	13	3.8	1.3	2.1	4.5
	B	20	5.2	1.4	3.6	6.5
	C	14	3.3	1.3	2.5	4.3
	D	10	1.7	1.0	1.5	2.5
Techado	1	35	9	1.8	5.2	10.5
	2	36	10	1.8	5.4	11.5

**Table S5. Average estimated paleointensity and associated uncertainties.** The first and second columns give the name of the meteorite and which K–T interface is considered. The third column shows the average declination and inclination obtained from bootstrapping. The fourth, fifth and sixth columns give the measurement uncertainty, small-number statistical uncertainty and uncertainty relating to the island size at 320°C, respectively (section S6). The total uncertainty in paleointensity is given in the seventh column. All uncertainties are the 95% confidence interval.

## S7. Phenomena that could affect the estimated paleointensities

### a) Magnetostatic interactions

As discussed on p. 218–219 of ref. (82), magnetostatic interactions can be added to the classic Néel picture (non-interacting single-domain particles) in the following way. Classically, thermoremanent magnetization ( $M_{\text{TRM}}$ ) at a temperature above the blocking temperature is given by Boltzmann statistics as:

$$M_{\text{TRM}} = M_{\text{RS}} \tanh\left(\frac{\mu_0 V M_S(T_B) H}{k_b T_B}\right) \quad (\text{S8})$$

where  $V$  is the volume of the particle,  $M_{\text{RS}}$  is the saturation remanence,  $M_S(T_B)$  the saturation magnetization at blocking temperature  $T_B$ ,  $H$  is the applied field,  $k_b$  the Boltzmann’s constant and  $\mu_0$  the vacuum permeability. Considering magnetostatic interactions, the applied field is  $H = H_{\text{ext}} + H_{\text{int}}$  where  $H_{\text{ext}}$  is the external field and  $H_{\text{int}}$  the interaction field. Except for rare spatial distribution of grains such as in a magnetotactic bacteria (lined up end to end),  $H_{\text{int}} < 0$ , which is expected in the CZ, given the spatial arrangement of the islands (Fig. S4A). This implies that for an observed  $M_{\text{TRM}}$ , one would underestimate the ambient field if one did not take into account interactions. Opposing signs of  $H_{\text{ext}}$  and  $H_{\text{int}}$  should also typically hold for thermochemical remanent magnetization for such a grain spatial distribution.

Micromagnetic simulations demonstrate that the CZ islands recorded remanence immediately after they chemically ordered to form tetrataenite. During this ordering, the

magnetocrystalline anisotropy increases dramatically, which causes the islands to adopt either a single domain state (if their magnetic easy axis coincides with their major axis— islands are ellipsoids) or, more likely, a two-domain state separated by a domain wall (24).

The NRM acquisition process is the object of active research. The results of micromagnetic simulations (68) support the idea that 1) the CZ does acquire a net NRM despite the existence of magnetostatic interactions and 2) this NRM is proportional to the external field strength, although the exact relationship between the field strength and the measured NRM remains under investigation. Independently from the case of the CZ, we can say that not accounting for magnetostatic interactions in almost any spatial configuration will result in an underestimation of the paleofield intensity. As a result, a Maxwell-Boltzmann approach is used to obtain a first-order approximation of the field intensities from average XMCD intensities in the CZ (eq. S5a–c).

Previous XPEEM measurements have provided two major pieces of evidence that the magnetostatic interactions between islands do not introduce spontaneous remanence into the CZ in the absence of an external field. The first piece of evidence for this is the unidirectional remanence observed across several K–T interfaces in this study and others (14, 69, 6:); it is extremely unlikely that a spontaneous remanence adopted by multiple K–T interfaces would be unidirectional.

The second argument is that if the CZ could spontaneously acquire its magnetization, one would expect to see a non-zero average XMCD intensity of the CZ in all XPEEM datasets ever acquired. This would result from the non-random magnetization of individual islands in the region of interest. However, field intensities indistinguishable from zero have been estimated from XPEEM measurements of two pallasites and two IAB iron meteorites (6:). One caveat of these analyses is that they were early on conducted for a single orientation of the sample with respect to the X-ray beam (as opposed to three in the most recent XPEEM studies including this one). It is possible for a region of interest to have an average XMCD intensity of zero for one rotation (see, for example, fig. S3) depending on the orientation of the individual magnetizations with respect to the X-ray beam. However, we argue that it seems unlikely, though not impossible, that all four measurements were conducted in a configuration such that images would all exhibit an average XMCD intensity of zero. We take this as an empirical evidence that weakly magnetized CZ exist, arguing also against the spontaneous acquisition of strong remanences.

Interactions between an assemblage of closely-packed magnetic grains can affect the magnitude of the remanent magnetization they adopt (27). Simulations of interacting grains with varying degrees of packing fraction demonstrate that the remanent magnetization in a tightly clustered, strongly interacting assemblage of particles could be an order of magnitude weaker than that adopted by particles that are spread far apart and therefore weakly interacting (27). As such, the closely packed nature of CZ islands suggests the paleointensity recovered from this intergrowth could be up to an order of magnitude higher than the intensity of the external field it experienced.

Finally, it should be noted that in the regions of interest (i.e., within 0.5  $\mu\text{m}$  of the rim for Techado and 2  $\mu\text{m}$  for Colomera), the local Ni content of the CZ is > 38 wt.%, which implies that by the time the CZ reached 320°C the islands were already > 70% of the present-day size in both meteorites (i.e., ~80–90 nm) (28). Given the presence of the interaction field and the very high field (> 1 T) needed to re-nucleate a domain wall in single-domain tetrataenite islands (24), the final growth of the islands from >70% to 100% of present-day size will not change their magnetization state.

### b) Field amplification

The IIEs cooled in a large reservoir of metal, which was very likely dominated by large multidomain kamacite grains like those present in IIE hand samples at the time that the CZ islands ordered to form tetrataenite. This implies that the field that magnetized the CZ islands may have had a non-negligible induced component resulting from the low magnetic coercivity of these multidomain grains. This component would have been recorded by the CZs and, if not accounted for, could yield an overestimation in our theoretical calculations of the actual magnetizing field (see main text). Here, we calculate the extent of such field amplification for the limiting cases of a spherical and a cylindrical geometry of the reservoir.

The total magnetic field inside a magnetized material ( $H_{\text{tot}}$ ) is the sum of the external magnetic field ( $H_{\text{ext}}$ ) and the demagnetizing magnetic field ( $H_d$ ). In one dimension, the demagnetizing field and the magnetization ( $M$ ) are related by a demagnetizing factor  $N$  ranging between 0 and 1 that depends on the shape of the material:

$$H_{\text{tot}} = H_{\text{ext}} - NM \quad (\text{S9})$$

Moreover, the magnetic induction inside ( $B_{\text{in}}$ ) and outside ( $B_{\text{ext}}$ ) the cylinder and the magnetic field are related by:

$$\begin{aligned} B_{\text{in}} &= \mu_0(H_{\text{tot}} + M) = \mu_r \mu_0 H_{\text{tot}} \\ B_{\text{ext}} &= \mu_0 H_{\text{ext}} \end{aligned} \quad (\text{S10})$$

where  $\mu_r$  is the relative magnetic permeability of the material and  $\mu_0$  is the permeability of free space. We can consider two end-member geometries to assess the effect of the demagnetizing field on the total field. For a sphere,  $N = 1/3$ , while for a cylinder of radius  $R$  and length  $L$  with the field oriented along its main axis (82):

$$N = 1 - \frac{L}{\sqrt{R^2 + L^2}} \quad (\text{S11})$$

which for an infinitely long cylinder gives  $N = 1$ . Inserting  $N = 1/3$  into eqs. (S9–S10), we obtain a relationship between the total field inside the material and the external field for a sphere:

$$B_{\text{in}} = \frac{3\mu_r}{\mu_r + 2} B_{\text{ext}} \quad (\text{S12a})$$

Inserting eq. (S11) into eqs. (S9–S10), we obtain the field inside an infinite cylinder:

$$B_{\text{in}} = \mu_r B_{\text{ext}} \quad (\text{S12b})$$

The relative permeability is related to the low-field magnetic susceptibility,  $\chi_{LF}$  as  $\mu_r = 1 + \chi_{LF}$ , which has been measured for more than 180 iron meteorites (92) and found to range between 1 and 20. Therefore, in the case where the IIE reservoir would have formed a long, thin metallic dike, the magnetic field estimated from the Maxwell-Boltzmann equation (eq. S5a–c) could overestimate the paleointensity by a factor of 20, which would result in minimum average field intensities of 0.8  $\mu\text{T}$  and 1.8  $\mu\text{T}$  for Colomera and Techado, respectively. If the IIE reservoir had a spherical shape, we would expect a minimal amplification by a factor of  $\sim 3$ , yielding minimum average paleointensities of 6  $\mu\text{T}$  and 12  $\mu\text{T}$  for Colomera and Techado, respectively.

### c) Impact-induced shock waves

Impact-induced shock waves can demagnetize minerals. However, meteoritic tetrataenite retains more than 97% of its saturation isothermal remanent magnetization at 1.2 GPa (73). Ref. (73) defines a median destructive stress, which corresponds to the stress needed to erase 50% of the remanent magnetization. This value can be extrapolated from their experimental data as long as there is no phase transition occurring in the mineral in the pressure range of interest. Such an extrapolation shows that the mean destructive stress derived for tetrataenite is above 13 GPa. Because this is the maximum pressure possibly experienced by Colomera and Techado (as indicated by the presence of light-shock-induced deformations of the kamacite—Neumann bands, main Fig. 2), the magnetization of the cloudy zones has not been substantially modified by shock.

### S8. Island size measurements for Colomera and Techado

We analyzed K–T interfaces A, B and C in Colomera after etching with 2% nital for 25 s using the Zeiss-Merlin high-resolution SEM in the Center for Material Science and Engineering at MIT. Interfaces were imaged with secondary electrons, a beam energy of 5 keV and a beam current of 50 pA. Images were analyzed using the FIJI software (74) (Fig. S4A). We first measured the island size within the 0.5- $\mu\text{m}$  closest to the tetrataenite rim. The sizes of 94 islands were measured for interface A, 69 for interface B, and 84 for interface C, with average sizes of  $126 \pm 4$  nm,  $125 \pm 4$  nm and  $128 \pm 3$  nm (2 s.e.), respectively. These are in agreement with a published value of  $123 \pm 2$  nm taken on a different subsample of Colomera (75). This was repeated for three consecutive 0.5- $\mu\text{m}$  wide regions away from the rim (covering a 2- $\mu\text{m}$  wide region in total). We found that the island size does not significantly decrease with distance to the rim within this region. Interface D was not measured; however, given the similarity in size and shape of this interface with the three others, as well as the narrow range of average sizes found for interfaces A, B and C, we assumed an average island size of 125 nm for this interface in our calculations.

To image the cloudy zone in Techado, we adopted a different approach using a dual beam method. We first imaged the boundary between the rim and the coarsest islands using secondary electrons produced by a Ga ion beam (30 kV and 9.7 pA) on a polished sample. This beam sputtered the surface of the sample, preferentially etching the matrix in the CZ, creating topographically high islands (Fig. S4B). A second image was then acquired using secondary electrons with a 5-keV and 170-pA beam (Fig. S4C). A total of 57 line profiles were taken parallel to the rim on several cloudy zones—including those analyzed with XPEEM—to estimate the size of the islands in the region of interest, with an average value of  $102 \pm 4$  nm (2- $\sigma$  uncertainty). In some regions of the cloudy zones, polishing led to the deposition of material shadowing the surrounding material from the ion beam. This resulted in large, unsputtered areas obscuring the islands beneath them, which we avoided during island size measurements. These measurements

were taken on a FEI Helios FIB-SEM at the Department of Materials Science and Metallurgy, University of Cambridge.

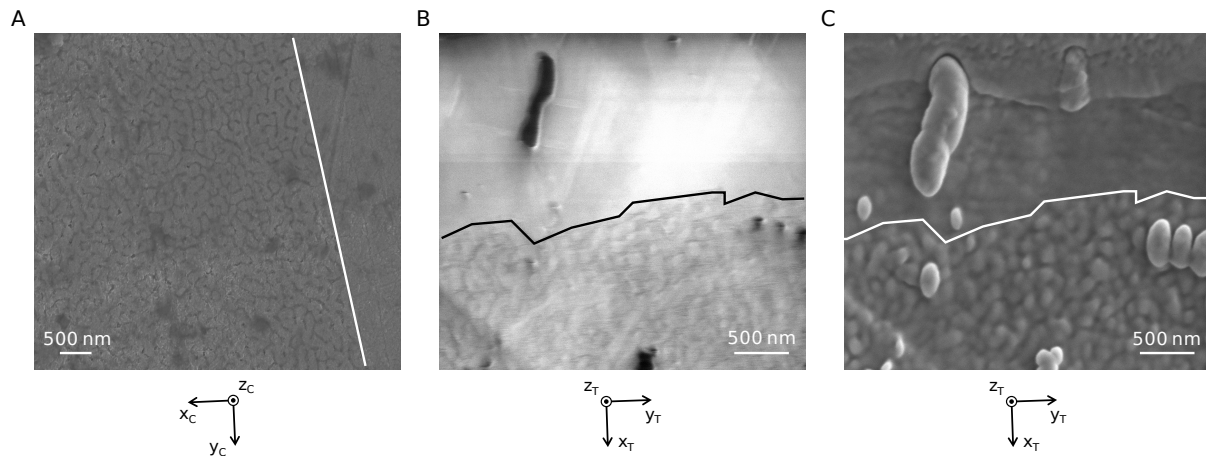


**Fig. S4 Island size measurements for Colomera.** (A) Secondary electron image of a region of cloudy zone in K–T interface C in Colomera. The separation between the cloudy zone and the tetraetaenite rim is delimited by a white line. The sample was polished down to a surface roughness of 0.3  $\mu\text{m}$  with a diamond paste and etched with 2% nital for 25 s. The reference frame refers to Fig. S3. (B) Secondary electron image of a region of cloudy zone in K–T interface 2 in Techado produced by a Ga ion beam. The separation between the cloudy zone and the tetraetaenite rim is delimited by a black line. (C) Secondary electron image of the same region after the Ga ion beam etched the sample.

### S9. Cloudy zone formation model

The CZ forms by spinodal decomposition, a diffusion-controlled phase separation that occurs spontaneously when an alloy becomes unstable to inherent fluctuations in composition (76). The Ni-rich taenite in iron meteorites, whose Ni content decreases with distance from the K–T interface, may undergo spinodal decomposition and form the CZ if the meteorite cools sufficiently slowly compared to the atomic diffusion timescale ( $\lesssim 5000^\circ\text{C My}^{-1}$ ). Next to the interface (where taenite is up to  $\sim 41$  wt.% Ni), spinodal decomposition occurs at  $\sim 360^\circ\text{C}$ . The formation temperature decreases with the local bulk Ni content of the cloudy zone.

We used a one-dimensional numerical model to simulate cloudy zone formation in the cooling environment of a meteorite parent body (28). The size of cloudy zone islands can be obtained at any temperature, providing a means of constraining the island size at  $320^\circ\text{C}$  when they acquired their remanence. Paleointensity estimates, as well as the small-number uncertainty on this estimate, depend on the size of the islands at this temperature (Section S6). Moreover, at the end of a simulation, the CZ island sizes are essentially equivalent to their present-day sizes. Consequently, the cooling rate of a meteorite at the CZ formation temperature can be estimated after measuring the average island size and Ni content of the coarse-island region of the CZ.

Using wavelength dispersive spectrometry (WDS) with  $\sim 1$ - $\mu\text{m}$  spatial resolution, we measured the average composition of the region of the CZ within 2  $\mu\text{m}$  of the rim approximately between 39 and 40 wt.% Ni for all CZs analyzed in Colomera, and between 38 and 40 wt.% within  $\sim 0.5$   $\mu\text{m}$  for the CZs in Techado (Fig. S5). Moreover, the average island size next to the tetraetaenite rim is  $125 \pm 4$  nm and  $102 \pm 4$  nm for Colomera and Techado, respectively (Section S8). Combining these measurements with the cloudy zone formation model, we estimate that Colomera and

Techado cooled below 350°C at  $2.5 \pm 1.4^\circ\text{C My}^{-1}$  and  $4.6 \pm 1.9^\circ\text{C My}^{-1}$ , respectively. In addition, given the measured local bulk composition (i.e., the composition of the region of interest in the CZ), we estimate that the islands were  $78 \pm 5\%$  of present-day size when they cooled through 320°C and acquired their magnetization. The WDS measurements were conducted on the JEOL-JXA-8200 Superprobe available in the Earth, Atmospheric and Planetary Science department at MIT, with a 15 keV, 1 nA electron beam.

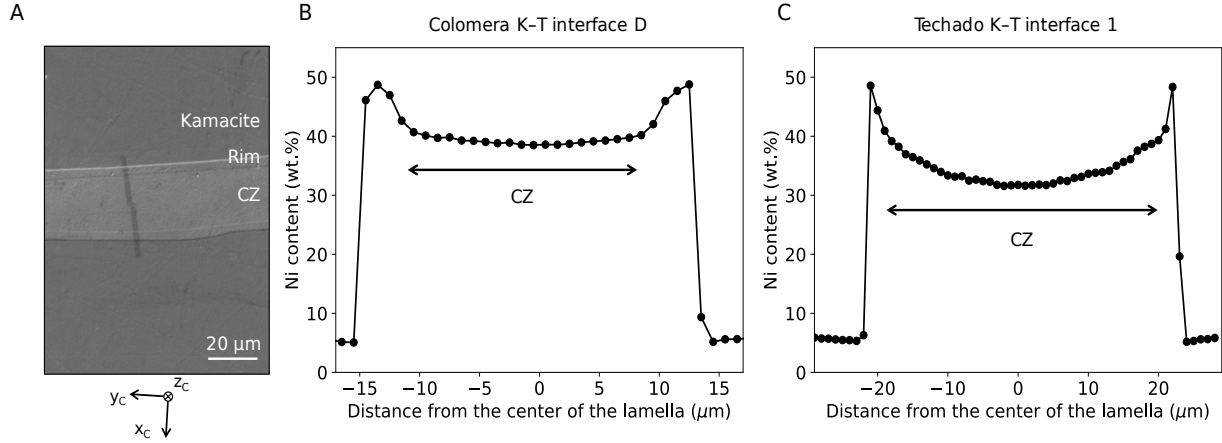


**Fig. S5. Ni-compositions across K-T interfaces in Colomera and Techado.** (A) Secondary electron image of Colomera's K-T interface D. The dark dots forming a line show where compositional measurements shown in (B) were taken. The reference frame refers to Fig. S3. (B) Ni content (in wt.%) across Colomera's K-T interface D. The approximate distance covered by the CZ is shown. The peak in Ni content in both sides of the CZ indicate the tetrataenite rim. The surrounding kamacite is also visible at ~5 wt.% Ni. (C) Same measurement across Techado's K-T interface 1.

### S10. Field intensity calculations

Assuming a dipole magnetic field generated by core dynamo activity, we calculated the intensity of the field expected at different depths in the silicate layer of the parent body. We considered two cases treated separately below: 1) a thermochemical convection dynamo powered by core solidification generating a magnetic field when the meteorites cooled through the tetrataenite blocking temperature and 2) a remanent crustal field resulting from the previous magnetization of the unmelted crust of the parent body. In both cases, we calculated the resulting field for a 170-km radius parent body with a 60-km radius metallic core (like the one used in our impact simulations) generating a dipole field with an origin at the body's center.

Assuming the dynamo is still active, the field intensity at the surface ( $B_{\text{surf}}$ ) is given by:

$$B_{\text{surf}} \sim d \left( \frac{R_{\text{core}}}{R_{\text{body}}} \right)^3 B_{\text{CMB,dip}} \quad (\text{S13})$$

where  $R_{\text{core}}$  and  $R_{\text{body}}$  are the radii of the metallic core and the planetesimal, respectively,  $B_{\text{CMB,dip}}$  is the dipole field at the core-mantle boundary (CMB). The  $d = 1/7$  factor is the ratio of the dipolar field strength to the total field strength at the top CMB for an Earth-like convection-

driven dynamo (77). A dipole field between 0.1 and 2500  $\mu\text{T}$  at the CMB generates a field between 0.0006 and 16  $\mu\text{T}$  at the surface of the body and a 0.002- to 60- $\mu\text{T}$  field midway through the silicate layer.

Assuming that the top 20 km of the body acquired a thermoremanent magnetization due to an early thermally-driven dynamo field, the crust's magnetization ( $M_{\text{TRM}}$ ) can be written as:

$$M_{\text{TRM}} \sim \frac{B_{\text{surf}} M_{rs}}{3 \times 10^{-3}} \quad (\text{S14})$$

where  $B_{\text{surf}}$  is the surface field in units of T (from eq. S13) and  $M_{rs}$  is the saturation remanence of the crust (78). The upper crust of the parent body must have cooled fast enough to acquire its magnetization while the thermally-driven dynamo was still active [i.e., less than 15 My after CAI-formation (37)]. Assuming an H-chondrite-like crust, we considered  $M_{rs}$  values of fast-cooled H chondrites. The H4 chondrites Forest Vale and Saint Marguerite cooled through  $\sim 600^\circ\text{C}$  at  $> 5000^\circ\text{C My}^{-1}$  (79) and have  $M_{rs}$  values of 0.03 and 0.06  $\text{A m}^{-1}$ , respectively (7:).

The crustal remanent field is then given by:

$$B_{\text{crust}} = \mu_0 \frac{4\pi}{3} \left( \frac{R_{\text{body}}^3 - [R_{\text{body}} - R_{\text{crust}}]^3}{[R_{\text{body}} - R_{\text{crust}}]^3} \right) M_{\text{TRM}} \quad (\text{S15})$$

where  $R_{\text{crust}}$  is the thickness of the magnetized silicate layer (7:). According to eqs. (S13–S15), if the crust recorded a field between 0.1 and 2500  $\mu\text{T}$  at the CMB, the intensity of the crustal remanent field would range between  $\sim 1 \times 10^{-8}$   $\mu\text{T}$  and 0.0003  $\mu\text{T}$ , which is orders of magnitude below the paleointensities measured from IIEs.

Unlike the calculated crustal field, the thermochemical dynamo field ranges within the same order of magnitude as our paleointensity estimate. With our current understanding of how the paleointensity is affected by magnetostatic interactions and amplification due to the high permeability of tetrataenite or surrounding kamacite (Section S7), this strongly favors the direct dynamo hypothesis. It should also be noted that an additional magnetic study of Forest Vale has shown that this meteorite is only capable of retaining an unstable low-coercivity ( $< 16$  mT) remanent magnetization (14), which strongly suggest that a Forest Vale-like IIE crust could not have preserved the record of an early dynamo long enough to be the source of the magnetic field recorded by Techado and Colomera.

Finally, it has been shown that to generate a dynamo powered by thermal convection, a planetesimal should be  $> 350$  km in radius (37). Our thermal evolution model suggests that the IIE parent body could have been much smaller ( $> 170$  km in radius; section S11). Although our simulations do not exclude the possibility of a larger parent body, they also favor the direct dynamo hypothesis.

## S11. Thermal model

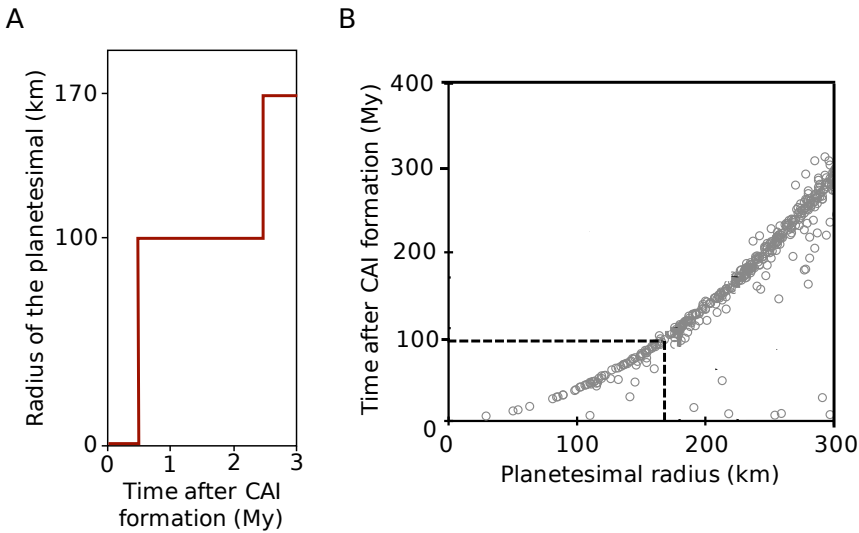


**Fig. S6. Accretion history and core crystallization of model planetesimal.** (A) Radius of a planetesimal,  $R_{\text{body}}$ , during its simulated accretion process, composed of two instantaneous accretion events and resulting in the formation of a 170-km radius, partially-differentiated object. Initial instantaneous accretion at 0.5 My after CAI-formation creates a planetesimal seed that differentiates into a liquid metallic core overlaid by a melted silicate mantle. This seed is covered instantaneously at 2.4 My after CAI-formation by cold material that does not differentiate and form a chondritic crust. (B) Time after which the latent heat resulting from the instantaneous solidification of the entire core at the Fe-S eutectic temperature ( $930^{\circ}\text{C}$ ) is extracted across the core-mantle boundary in a 1D simulation of a planetesimal's accretion and thermal evolution, based on ref. (37). Dotted lines show the minimum size of the parent body for which the core crystallization is completed only after Colomera recorded a field,  $\sim 97$  My after CAI-formation.

## S12. Impact simulations

The objective of our impact simulations is to demonstrate, using two representative scenarios, the feasibility of an impact-induced formation of the IIEs. The results of these simulations are analyzed in light of three major experimental constraints:

1. A liquid core has to be preserved to allow a magnetic field to be generated at a later time;
2. Molten silicates have to be exposed to near-surface temperatures;
3. The created IIE reservoir has to be buried in the upper half of the silicate layer of the body.

We also briefly show how the two selected scenarios can be compatible with textural features resulting from the mixing of metal and silicates found in the IIEs. Note that our simulations are not meant to find the specific set of impact conditions that could have formed a IIE reservoir on a partially-differentiated parent body. They should be considered as a proof-of-concept.

Composition of impactor	Time of impact (My after CAI-formation)	Radius of impactor (km)	Impact velocity (km s <sup>-1</sup> )
Iron	10	30	1, 2, 3, 4, 5
	30	10	1, 2, 3, 4
		20	1, 2, 3, 4
		30	1, 2, 3
Dunite	30	40	3, 4, 5, 6, 9

**Table S6. Summary of the sets of initial conditions investigated in the impact simulations.** The first column shows the nature of the impactor, the second column gives the time of the impact, the third column is the radius of the impactor and the fourth column is the impact velocity.

From the suite of simulations conducted with a 30-km radius metallic impactor at 30 My, it appears that the implantation of metal into the target during a vertical impact requires impact velocities  $\leq 1$  km s<sup>-1</sup>. The iron impactor merges into the core at velocities  $\geq 2$  km s<sup>-1</sup>. However, one of our simulations shows that a smaller, 10-km radius impactor could be implanted when impacting at  $\geq 4$  km s<sup>-1</sup> (Fig. S7A). We discuss how the impact velocity would likely increase with a decreasing impactor radius in Section S13. The texture and arrangement of silicate and metal grains in the IIEs suggest the metal was partly solid during mixing (18). In this iron impactor scenario, the marginal heating ( $< 100^\circ\text{C}$ ) of the exogenous metal during impact could explain silicate mixing with solid, ductile Fe-Ni, while the thermal re-equilibration could have allowed the metal to partially melt after the impact.

On the other hand, we found that collisions involving a chondritic impactor of 40 km in radius can sometimes excavate small amounts of core material into the mantle. We find such a result for impacts with a 40-km radius body at 4 and 5 km s<sup>-1</sup> (main text Fig. 6A–B). The range of impact energies needed for this outcome is relatively narrow as impacts at 3 and 6 km s<sup>-1</sup> do not produce similar results (Fig. S7B). Higher energy impacts fully break up the core, leaving no central core, and lower energy impacts fail to excavate core material.

Head-on impacts are less likely than impacts at an angle with respect to the normal to the surface of the target, with 45° being the most probable configuration (: 2). Such oblique impacts were not explored here as they necessitate more computationally expensive three-dimensional simulations while we were only interested in a proof of concept that exogenous and/or endogenous metal can be implanted in the silicate layer of a partially-differentiated planetesimal. However, three-dimensional iSALE simulations of non-vertical impacts onto non-differentiated planetesimals have shown that impacting at an angle shallower than vertical yields less heating and less material excavation for the same impact velocity (83). Oblique impacts may therefore allow for faster impactors than those used in our simulations for a similar implantation of exogenous iron or excavation of endogenous iron into the mantle. One limitation to highly oblique impacts would be that the amount of material from the impactor effectively accreted during these collisions significantly decreases.

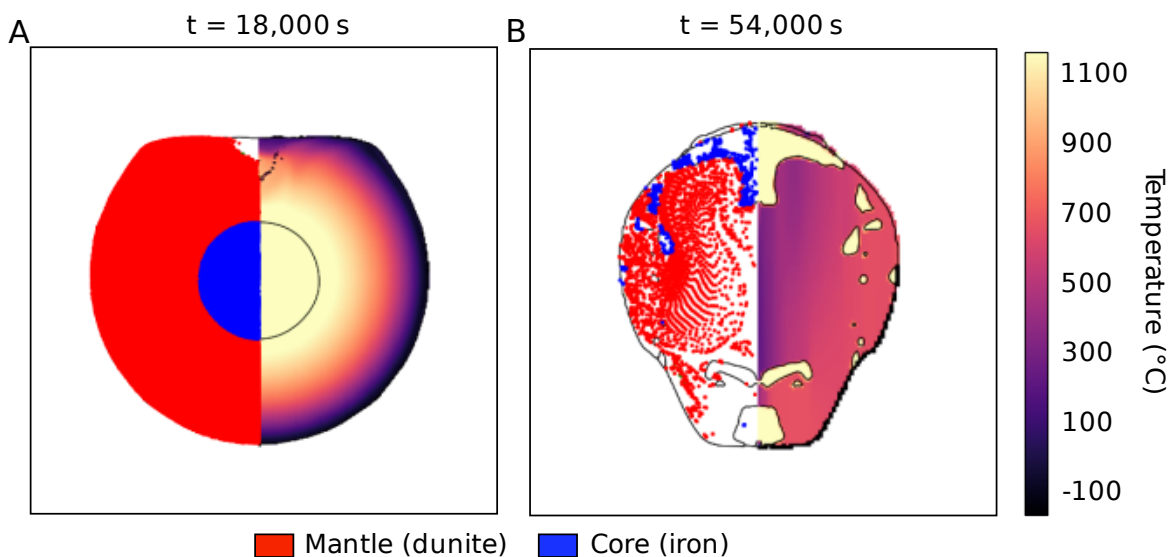


**Fig. S7. Outcomes of additional impact simulations using iSALE-Dellen.** (A) End of the impact simulation after 18,000 s for a 10-km radius, pure iron impactor impacting vertically at 4 km s<sup>-1</sup>. The left half of the figure shows the constituent materials, and the right half shows the temperature in the target and impactor. Small amounts of projectile material are identifiable in the upper half of the target's silicate layer. A finite number of tracers was used to identify the different materials on the left half of the figure; the impact may result in areas where no tracers are present (white), but it does not mean no material is present. (B) End of the impact simulation after 54,000 s for a 40-km radius, pure dunite impactor impacting vertically at 6 km s<sup>-1</sup>. The core is scattered in the outer layers of the target leaving no central or dominant metal reservoir for the dynamo activity to likely occur.

### S13. Scaling of the impact parameters

In this section, we estimate from cratering scaling laws how small an impactor could be to yield a similar outcome as the simulations we conducted (section S12). We are motivated by the fact that the early population of the inner solar system was likely dominated by objects < 10 km in radius (i.e., smaller than the 30-km radius body we simulated) and impact velocities ranging between 5 and 15 km s<sup>-1</sup> (40).

Scaling laws have been developed and widely used to scale the outcomes of a laboratory experiment to a planetary impact or infer impact and impactor properties from crater observations (84). These scaling laws in theory do not extend to the type of outcomes we are studying in this paper (i.e., implantation of metal or core excavation). However, in the absence of other means to efficiently investigate the outcomes of such events as a function of impactor size and impact velocity, we assumed these scaling laws approximately apply to our problem. In the strength regime, the impactor radius ( $R_{\text{imp}}$ ) and velocity ( $v_{\text{imp}}$ ) are related by:

$$R_{\text{imp}}^3 v_{\text{imp}}^2 = \text{constant} \quad (\text{S16})$$

where the constant contains information about the target density, impactor mass, target strength and outcome (successful implantation and excavation; in theory, crater volume). With the simulations we conducted, we find that a 30-km radius iron impactor can be implanted at  $1 \text{ km s}^{-1}$ ; on the other hand, a 40-km radius chondritic impactor can excavate core material permanently if the impact occurs at  $5 \text{ km s}^{-1}$ . This allows us to estimate the constant in both cases. We find that iron impactors as small as 5 km in radius could be efficiently implanted for a velocity of  $15 \text{ km s}^{-1}$ , while for the same velocity, a 20-km radius chondritic impactor would be needed to excavate part of the parent's core (Fig. S8). Note that for the iron impactor scenario, this approximation suggests that a 10-km radius impactor would be implanted for an impact velocity of  $\sim 5 \text{ km s}^{-1}$ , which is in good agreement with the simulations we conducted (Section S12).

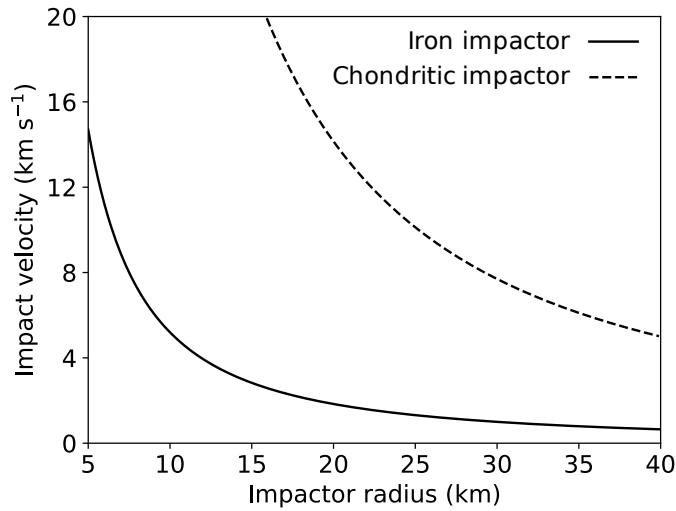


**Fig. S8. Conditions required to emplace metal into the mantle of the target.** Estimated impact velocity required for a given impactor radius to obtain the same crater volume with either permanent implantation of an iron impactor (solid line) or excavation of core material by a chondritic impactor (dashed lines).

#### S14. Likelihood of the IIE-forming impact

Here, we seek to establish whether our IIE-forming impact scenarios (sections S12–S13) are compatible with the size distributions and impact velocity distributions provided by collisional evolution models.

First, we note that IIE irons isotopically fall within the non-carbonaceous chondrite clan (85). This indicates that the IIEs formed in the terrestrial-planet region or asteroid belt; they are not likely the byproduct of an impact between an asteroid and an outer solar system body. Second, the number of impacts ( $N_{\text{imp}}$ ) on the IIE parent body can be written as:

$$N_{\text{imp}} \sim P_i (R_{\text{target}} + R_{\text{proj}})^2 N_{\text{proj}} t_{\text{imp}} \quad (\text{S17})$$

where  $R_{\text{target}}$  and  $R_{\text{proj}}$  are the radii of the target and projectile in km, respectively,  $N_{\text{proj}}$  is the number of potential projectiles required to have  $N_{\text{imp}}$  impacts,  $t_{\text{imp}}$  is the time of the impact relative to CAI formation and  $P_i$  is the intrinsic collision probability between the projectiles and the target body (84).

To produce the IIEs, we need at least one impact ( $N_{\text{imp}} = 1$ ). For main belt bodies striking main belt bodies,  $P_i$  is probably of the order of  $3 \times 10^{-18} \text{ km}^{-2} \text{ yr}^{-1}$  (85). Therefore, if the impact occurred at 30 My after CAI-formation, assuming a 10-km radius projectile and a 170-km radius target, we get  $N_{\text{proj}} = 3.5 \times 10^5$ . This is approximately 200 times the current population of the main asteroid belt with  $\geq 10$ -km radius and is roughly equivalent to the entire early population predicted in this region (84). Such substantial small body population lasting for 30 My would undergo extensive collisional evolution. It would not only decimate the  $\geq 10$ -km radius asteroid population, but would also yield a main belt size-frequency distribution that looks very different than the observed one (41). Therefore, it seems improbable that the IIE-forming impact could occur in the main belt region.

One way to overcome low collision probabilities and small populations is to move the impact to the terrestrial planet region. For example, the ejecta produced by the Moon-forming giant impact have a probability  $P_i = 190 \times 10^{-18} \text{ km}^{-2} \text{ yr}^{-1}$  of hitting one another (42). Using this value in eq. (S17), we get  $N_{\text{proj}} \sim 5,500$ . This number could have been achieved as a byproduct of terrestrial planet formation. In this region, at  $> 30$  Myr after CAI-formation, models indicate numerous protoplanets were colliding with one another, with the largest event represented by a roughly Mars-size impactor slamming into the proto-Earth to make the Moon (42). These events should have produced an abundance of iron-rich debris, some which could have struck the IIE parent body if it was located within the same approximate zone.

Another alternative to explain how endogenous metal could have impacted the IIE parent body is to consider subsequent grazing impacts, where one or several hit-and-run impacts (86) would have stripped the mantle of a differentiated impactor dynamically bound to the target, eventually resulting in an impact between an iron-rich, small object and the undisrupted target. However, this concept has until now only been suggested for giant impact involving planetary embryos that are much larger than the IIE parent body (87).

## REFERENCES AND NOTES

1. A. N. Krot, K. Keil, E. R. D. Scott, C. A. Goodrich, M. K. Weisberg, Classification of meteorites and their genetic relationships, in *Treatise on Geochemistry*, H. D. Holland, K. K. Turekian, Eds. (Elsevier, 2014), vol. 1, pp. 1–63.
2. B. Mason, Meteorites. *Am. Sci.* **55**, 429–455 (1967).
3. P. J. Hevey, I. S. Sanders, A model for planetesimal meltdown by  $^{26}\text{Al}$  and its implications for meteorite parent bodies. *Meteorit. Planet. Sci.* **41**, 95–106 (2006).
4. E. R. D. Scott, Meteoritical and dynamical constraints on the growth mechanisms and formation times of asteroids and Jupiter. *Icarus* **185**, 72–82 (2006).
5. A. Johansen, M.-M. Mac Low, P. Lacerda, M. Bizzarro, Growth of asteroids, planetary embryos, and Kuiper belt objects by chondrule accretion. *Sci. Adv.* **1**, e1500109 (2015).
6. S. J. Weidenschilling, Accretion of the asteroids: Implications for their thermal evolution. *Meteorit. Planet. Sci.* **54**, 1115–1132 (2019).
7. L. T. Elkins-Tanton, B. P. Weiss, M. T. Zuber, Chondrites as samples of differentiated planetesimals. *Earth Planet. Sci. Lett.* **305**, 1–10 (2011).
8. B. P. Weiss, L. T. Elkins-Tanton, Differentiated planetesimals and the parent bodies of chondrites. *Annu. Rev. Earth Planet. Sci.* **41**, 529–560 (2013).
9. A. J. Irving, T. E. Larson, F. J. Longstaffe, D. Rumble, T. E. Bunch, J. H. Wittke, S. M. Kuehner, A primitive achondrite with oxygen isotopic affinities to CV chondrites: Implications for differentiation and size of the CV parent body, paper presented at the 85th American Geophysical Union Fall Meeting, San Francisco, CA, 2004.
10. A. W. Tait, A. G. Tomkins, B. M. Godel, S. A. Wilson, P. Hasalova, Investigation of the H7 ordinary chondrite, Watson 012: Implications for recognition and classification of Type 7 meteorites. *Geochim. Cosmochim. Acta* **134**, 175–196 (2014).

11. L. Carporzen, B. P. Weiss, L. T. Elkins-Tanton, D. L. Shuster, D. Ebel, J. Gattacceca, Magnetic evidence for a partially differentiated carbonaceous chondrite parent body. *Proc. Natl. Acad. Sci. U.S.A.* **108**, 6386–6389 (2011).
12. J. Gattacceca, B. P. Weiss, M. Gounelle, New constraints on the magnetic history of the CV parent body and the solar nebula from the Kaba meteorite. *Earth Planet. Sci. Lett.* **455**, 166–175 (2016).
13. J. Shah, H. C. Bates, A. R. Muxworthy, D. C. Hezel, S. S. Russell, M. J. Genge, Long-lived magnetism on chondrite parent bodies. *Earth Planet. Sci. Lett.* **475**, 106–118 (2017).
14. J. F. J. Bryson, B. P. Weiss, B. Getzin, J. N. H. Abrahams, F. Nimmo, A. Scholl, Paleomagnetic evidence for a partially differentiated ordinary chondrite parent asteroid. *J. Geophys. Res. Planets* **129**, 1880–1898 (2019).
15. C. Cournède, J. Gattacceca, P. Rochette, D. L. Shuster, Paleomagnetism of Rumuruti chondrites suggests a partially differentiated parent body. *Earth Planet. Sci. Lett.* **533**, 116042 (2020).
16. T. E. Bunch, E. Olsen, Potassium feldspar in Weekeroo Station, Kodaikanal, and Colomera iron meteorites. *Science* **160**, 1223–1225 (1968).
17. G. J. Wasserburg, H. G. Sanz, A. E. Bence, Potassium-feldspar phenocrysts in the surface of Colomera, and iron meteorite. *Science* **161**, 684–687 (1968).
18. A. Ruzicka, Silicate-bearing iron meteorites and their implications for the evolution of asteroidal parent bodies. *Geochemistry* **74**, 3–48 (2014).
19. K. H. McDermott, R. C. Greenwood, E. R. D. Scott, I. A. Franchi, M. Anand, Oxygen isotope and petrological study of silicate inclusions in IIE iron meteorites and their relationship with H chondrites. *Geochim. Cosmochim. Acta* **173**, 97–113 (2016).
20. J. T. Wasson, Formation of non-magmatic iron-meteorite group IIE. *Geochim. Cosmochim. Acta* **197**, 396–416 (2017).

21. B. P. Weiss, J. Gattacceca, S. Stanley, P. Rochette, U. R. Christensen, Paleomagnetic records of meteorites and early planetesimal differentiation. *Space Sci. Rev.* **152**, 341–390 (2010).
22. R. Blukis, R. Rüffer, A. I. Chumakov, R. J. Harrison, A high spatial resolution synchrotron Mössbauer study of the Tazewell III CD and Esquel pallasite meteorites. *Meteorit. Planet. Sci.* **52**, 925–936 (2017).
23. C. W. Yang, D. A. Williams, J. I. Goldstein, A revision of the Fe-Ni phase diagram at low temperatures ( $< 400^{\circ}\text{C}$ ). *J. Phase Equilib.* **17**, 522–531 (1996).
24. J. F. Einsle, A. S. Eggeman, B. H. Martineau, Z. Saghi, S. M. Collins, R. Blukis, P. A. J. Bagot, R. J. Harrison, Nanomagnetic properties of the meteorite cloudy zone. *Proc. Natl. Acad. Sci. U.S.A.* **115**, E11436–E11445 (2018).
25. M. Uehara, J. Gattacceca, H. Leroux, D. Jacob, C. J. van der Beek, Magnetic microstructures of metal grains in equilibrated ordinary chondrites and implications for paleomagnetism of meteorites. *Earth Planet. Sci. Lett.* **306**, 241–252 (2011).
26. A. Scholl, H. Ohldag, F. Nolting, J. Stöhr, H. A. Padmore, X-ray photoemission electron microscopy, a tool for the investigation of complex magnetic structures (invited). *Rev. Sci. Instrum.* **73**, 1362–1366 (2002).
27. R. J. Harrison, I. Lascu, FORCulator: A micromagnetic tool for simulating first-order reversal curve diagrams. *Geochem. Geophys. Geosyst.* **15**, 4671–4691 (2014).
28. C. Maurel, B. P. Weiss, J. F. J. Bryson, Meteorite cloudy zone formation as a quantitative indicator of paleomagnetic field intensities and cooling rates on planetesimals. *Earth Planet. Sci. Lett.* **513**, 166–175 (2019).
29. J. Yang, J. I. Goldstein, Magnetic contribution to the interdiffusion coefficients in bcc ( $\alpha$ ) and fcc ( $\gamma$ ) Fe-Ni alloys. *Metall. Mater. Trans. A* **35**, 1681–1690 (2004).
30. W. S. Cassata, P. R. Renne, Systematic variations of argon diffusion in feldspars and implications for thermochronometry. *Geochim. Cosmochim. Acta* **112**, 251–287 (2013).

31. D. D. Bogard, D. H. Garrison, T. J. McCoy, Chronology and petrology of silicates from IIE iron meteorites: Evidence of a complex parent body evolution. *Geochim. Cosmochim. Acta* **64**, 2133–2154 (2000).
32. E. Dos Santos, J. Gattacceca, P. Rochette, G. Fillion, R. B. Scorzelli, Kinetics of tetrataenite disordering. *J. Magn. Magn. Mater.* **375**, 234–241 (2015).
33. H. Wang, B. P. Weiss, X.-N. Bai, B. G. Downey, J. Wang, J. Wang, C. Suavet, R. R. Fu, M. E. Zucolotto, Lifetime of the solar nebula constrained by meteorite paleomagnetism. *Science* **355**, 623–627 (2017).
34. R. Oran, B. P. Weiss, O. Cohen, Were chondrites magnetized by the early solar wind? *Earth Planet. Sci. Lett.* **492**, 222–231 (2018).
35. L. L. Hood, N. A. Artemieva, Antipodal effects of lunar basin-forming impacts: Initial 3D simulations and comparisons with observations. *Icarus* **193**, 485–502 (2008).
36. M. G. Sterenborg, J. W. Crowley, Thermal evolution of early solar system planetesimals and the possibility of sustained dynamos. *Phys. Earth Planet. Inter.* **214**, 53–73 (2013).
37. J. F. J. Bryson, J. A. Neufeld, F. Nimmo, Constraints on asteroid magnetic field evolution and the radii of meteorite parent bodies from thermal modelling. *Earth Planet. Sci. Lett.* **521**, 68–78 (2019).
38. F. Nimmo, Energetics of asteroid dynamos and the role of compositional convection. *Geophys. Res. Lett.* **36**, L10201 (2009).
39. H. J. Melosh, E. V. Ryan, E. Asphaug, Dynamic fragmentation in impacts: Hydrocode simulation of laboratory impacts. *J. Geophys. Res.* **97**, 14735–14759 (1992).
40. T. M. Davison, D. P. O'Brien, F. J. Ciesla, G. S. Collins, The early impact histories of meteorite parent bodies. *Meteorit. Planet. Sci.* **48**, 1894–1918 (2013).

41. W. F. Bottke Jr., D. D. Durda, D. Nesvorný, R. Jedicke, A. Morbidelli, D. Vokrouhlický, H. F. Levison, Linking the collisional history of the main asteroid belt to its dynamical excitation and depletion. *Icarus* **179**, 63–94 (2005).
42. W. F. Bottke, D. Vokrouhlický, S. Marchi, T. Swindle, E. R. D. Scott, J. R. Weirich, H. Levison, Dating the Moon-forming impact event with asteroidal meteorites. *Science* **348**, 321–323 (2015).
43. S. M. Brown, L. T. Elkins-Tanton, Compositions of Mercury's earliest crust from magma ocean models. *Earth Planet. Sci. Lett.* **286**, 446–455 (2009).
44. S. N. Raymond, A. Izidoro, The empty primordial asteroid belt. *Sci. Adv.* **3**, e1701138 (2017).
45. W. F. Bottke, D. Nesvorný, R. E. Grimm, A. Morbidelli, D. P. O'Brien, Iron meteorites as remnants of planetesimals formed in the terrestrial planet region. *Nature* **439**, 821–824 (2006).
46. S. Fornasier, B. E. Clark, E. Dotto, A. Migliorini, M. Ockert-Bell, M.A. Barucci, Spectroscopic survey of M-type asteroids. *Icarus* **210**, 655–673 (2010).
47. L. T. Elkins-Tanton, E. Asphaug, J. F. Bell III, D. Bercovici, B. G. Bills, R. P. Binzel, W. F. Bottke, M. Brown, J. Goldsten, R. Jaumann, I. Jun, D. J. Lawrence, P. Lord, S. Marchi, T. Mc Coy, D. Oh, R. Park, P. N. Peplowski, C. A. Polanskey, D. Potter, T. H. Prettyman, C. A. Raymond, C. T. Russell, S. Scott, H. Stone, K. G. Sukhatme, N. Warner, B. P. Weiss, D. D. Wenkert, M. Wieczorek, D. Williams, M. T. Zuber, Asteroid (16) Psyche: Visiting a metal world, paper presented at the 48th Lunar Planetary Science Conference, The Woodlands, TX, 2017.
48. J. Stöhr, H. A. Padmore, S. Anders, T. Stammler, Principles of X-ray magnetic dichroism spectromicroscopy. *Surf. Rev. Lett.* **5**, 1297–1308 (1998).
49. N. Van Roosbroek, L. Pittarello, A. Greshake, V. Debaille, P. Claeys, First finding of impact melt in the IIE Netschaëvo meteorite. *Meteorit. Planet. Sci.* **51**, 372–389 (2016).
50. D. L. Cook, R. J. Walker, M. F. Horan, J. T. Wasson, J. W. Morgan, Pt-Re-Os systematics of group IIAB and IIIAB iron meteorites, *Geochim. Cosmochim. Acta* **68**, 1413–1431 (2004).

51. K. Wünnemann, G. S. Collins, H. J. Melosh, A strain-based porosity model for use in hydrocode simulations of impacts and implications for transient crater growth in porous targets. *Icarus* **180**, 514–527 (2006).
52. G. S. Collins, H. J. Melosh, B. A. Ivanov, Modeling damage and deformation in impact simulations. *Meteorit. Planet. Sci.* **39**, 217–231 (2004).
53. T. M. Davison, F. J. Ciesla, G. S. Collins, Post-impact thermal evolution of porous planetesimals. *Geochim. Cosmochim. Acta* **95**, 252–269 (2012).
54. T. S. Kruijer, T. Kleine, Age and origin of IIE iron meteorites inferred from Hf-W chronology. *Geochim. Cosmochim. Acta* **262**, 92–103 (2019).
55. R. J. Lyons, T. J. Bowling, F. J. Ciesla, T. M. Davison, G. S. Collins, The effects of impacts on the cooling rates of iron meteorites, *Meteorit. Planet. Sci.* **54**, 1604–1618 (2019).
56. A. M. Ruzicka, M. Hutson, Comparative petrology of silicates in the Udei Station (IAB) and Miles (IIE) iron meteorites: Implications for the origin of silicate-bearing irons. *Geochim. Cosmochim. Acta* **74**, 394–433 (2010).
57. H. Takeda, W. Hsu, G. R. Huss, Mineralogy of silicate inclusions of the Colomera IIE iron and crystallization of Cr-diopside and alkali feldspar from a partial melt. *Geochim. Cosmochim. Acta* **67**, 2269–2287 (2003).
58. A. M. Ruzicka, G. W. Fowler, G. A. Snyder, M. Prinz, J. J. Papike, L. A. Taylor, Petrogenesis of silicate inclusions in the Weekeroo Station IIE iron meteorite: Differentiation, remelting, and dynamic mixing. *Geochim. Cosmochim. Acta* **63**, 2123–2143 (1999).
59. J. I. Goldstein, E. R. D. Scott, N. L. Chabot. Iron meteorites: Crystallization, thermal history, parent bodies, and origin. *Geochemistry* **69**, 293–325 (2009).
60. D. J. Dunlop, Ö. Özdemir, *Rock Magnetism: Fundamentals and Frontiers* (Cambridge Univ. Press, 1997), pp. 1–573.

61. J. F. J. Bryson, J. Herrero-Albillos, F. Kronast, M. Ghidini, S. A. T. Redfern, G. van der Laan, R. J. Harrison, Nanopaleomagnetism of meteoritic Fe-Ni studied using X-ray photoemission electron microscopy. *Earth Planet. Sci. Lett.* **396**, 125–133 (2014).
62. G. S. Watson, A test for randomness of directions. *Geophys. J. Int.* **7**, 160–161 (1956).
63. G. S. Watson, Large sample theory of the Langevin distribution. *J. Stat. Plan. Infer.* **8**, 245–256 (1983).
64. N. I. Fisher, T. Lewis, B. J. J. Embleton, *Statistical Analysis of Spherical Data* (Cambridge Univ. Press 1987), chap. 5.
65. T. Berndt, A. R. Muxworthy, K. Fabian, Does size matter? Statistical limits of paleomagnetic field reconstruction from small rock specimens. *J. Geophys. Res.* **121**, 15–26 (2016).
66. S. Yeem, R. J. Harrison, Interaction-driven domain-state transition in the meteorite cloudy zone: A hybrid micromagnetic approach to modelling remanence acquisition, paper presented at the AGU Fall Meeting, San Francisco, CA, 2019.
67. J. F. J. Bryson, C. I. O. Nichols, J. Herrero-Albillos, F. Kronast, T. Kasama, H. Alimadadi, G. van der Laan, F. Nimmo, R. J. Harrison, Long-lived magnetism from solidification-driven convection on the pallasite parent body. *Nature* **517**, 472–475 (2015).
68. J. F. J. Bryson, B. P. Weiss, R. J. Harrison, J. Herrero-Albillos, F. Kronast, Paleomagnetic evidence for dynamo activity driven by inward crystallisation of a metallic asteroid. *Earth Planet. Sci. Lett.* **472**, 152–163 (2017).
69. C. I. O. Nichols, J. F. J. Bryson, R. Blukis, J. Herrero-Albillos, F. Kronast, R. Rüffer, A. I. Chumakov, R. J. Harrison, Variations in the magnetic properties of meteoritic cloudy zone. *Geochem. Geophys. Geosyst.* **21**, e2019GC008798 (2020).
70. M. Terho, L. J. Pesonen, I. T. Kukkonen, *The Petrophysical Classification of Meteorites: New Results* (Report Q29.1/91/1, Geological Survey of Finland, 1993), pp. 1–68.

71. N. S. Bezaeva, J. Gattacceca, P. Rochette, R. A. Sadykov, V. I. Trukhin, Demagnetization of terrestrial and extraterrestrial rocks under hydrostatic pressure up to 1.2 GPa. *Phys. Earth Planet. Inter.* **179**, 7–20 (2010).
72. J. Schindelin, I. Arganda-Carreras, E. Frise, V. Kaynig, M. Longair, T. Pietzsch, S. Preibisch, C. Rueden, S. Saalfeld, B. Schmid, J.-Y. Tinevez, D. J. White, V. Hartenstein, K. Eliceiri, P. Tomancak, A. Cardona, Fiji: An open-source platform for biological-image analysis. *Nat. Methods* **9**, 676–682 (2012).
73. E. R. D. Scott, J. I. Goldstein, Thermal histories and origins of group IIE and IAB iron meteorites and their parent asteroids, paper presented at the 47th Lunar and Planetary Science Conference, The Woodlands, TX, 2016.
74. D. Porter, K. Easterling, M. Sherif, *Phase Transformations in Metals and Alloys* (CRC Press, ed. 3, 2004), chap. 5.
75. U. R. Christensen, V. Holzwarth, A. Reiners, Energy flux determines magnetic field strength of planets and stars. *Nature* **457**, 167–169 (2009).
76. J. Gattacceca, P. Rochette, Toward a robust normalized magnetic paleointensity method applied to meteorites, *Earth Planet. Sci. Lett.* **227**, 377–393 (2004).
77. E. R. D. Scott, T. V. Krot, J. I. Goldstein, S. Wakita, Thermal and impact history of the H chondrite parent asteroid during metamorphism: Constraints from metallic Fe–Ni, *Geochim. Cosmochim. Acta* **136**, 13–37 (2014).
78. J. Gattacceca, C. Suavet, P. Rochette, B. P. Weiss, M. Winklhofer, M. Uehara, J. M. Friedrich, Metal phases in ordinary chondrites: Magnetic hysteresis properties and implications for thermal history. *Meteorit. Planet. Sci.* **49**, 652–676 (2014).
79. C. I. O. Nichols, J. F. J. Bryson, J. Herreros-Albillos, F. Konrath, F. Nimmo, R. J. Harrison, Pallasite paleomagnetism: Quiescence of a core dynamo. *Earth Planet. Sci. Lett.* **441**, 103–112 (2016).

80. E. M. Shoemaker, Interpretation of lunar craters, in *Physics and Astronomy of the Moon*, Z. Kopal, Ed. (Academic Press, 1961), pp. 283–359.
81. T. M. Davison, F. J. Ciesla, G. S. Collins, D. Elbeshausen, The effect of impact obliquity on shock heating in planetesimal collisions. *Meteorit. Planet. Sci.* **49**, 2252–2265 (2014).
82. K. A. Holsapple, The scaling of impact processes in planetary sciences, *Annu. Rev. Earth Planet. Sci.* **21**, 333–373 (1993).
83. T. S. Kruijer, C. Burkhardt, G. Budde, T. Kleine, Age of Jupiter inferred from the distinct genetics and formation times of meteorites, *Proc. Natl. Acad. Sci. U.S.A.* **114**, 6712–6716 (2017).
84. W. F. Bottke Jr., D. D. Durda, D. Nesvorny, R. Jedicke, A. Morbidelli, D. Vokrouhlicky, H. Levison, The fossilized size distribution of the main asteroid belt. *Icarus* **175**, 111–140 (2005).
85. W. F. Bottke Jr., M. C. Nolan, R. Greenberg, R. A. Kolvoord, Velocity distributions among colliding asteroids. *Icarus* **107**, 255–268 (1994).
86. E. Asphaug, C. B. Agnor, Q. Williams, Hit-and-run planetary collisions. *Nature* **439**, 155–160 (2006).
87. A. Emsenhuber, E. Asphaug, Fate of the runner in hit-and-run collisions. *Astrophys. J.* **875**, 95 (2019).